EES Solar

PAPER

View Article Online
View Journal | View Issue

Cite this: *EES Sol.*, 2025, **1**, 1126

Large-area close-space sublimation enables the fabrication of efficient and stable perovskite solar cells

Inma Gomar-Fernández, Lidón Gil-Escrig,* Nathan Rodkey, Federico Ventosinos, Maximiliano Senno, Cristina Roldán-Carmona, Vladimir Held, Michele Sessolo and Henk J. Bolink *

Received 5th September 2025
Accepted 3rd October 2025

DOI: 10.1039/d5el00145e

rsc.li/EESSolar

Perovskite solar cells (PSCs) exhibit remarkable efficiency and versatility in fabrication methods. In this work, we present methylammonium lead iodide (MAPI) perovskite films deposited using a large-area close-space sublimation (CSS) technique. The large-area CSS system used here enables the simultaneous conversion of multiple samples under moderate vacuum conditions (1 mbar), offering a scalable and simple alternative to other high-vacuum techniques. The perovskite films have large grains and uniformly cover the substrate. These CSS prepared films lead to solar cells with a power conversion efficiency (PCE) of 18.8%. The solar cells have extraordinary stability, and they retain 90% of their initial efficiency after operating for 1000 hours at their maximum power point at 75 °C and under 1 sun illumination. The results highlight the potential of CSS as a scalable and simple method to produce high-quality perovskite films.

Broader context

The rapid rise of perovskite solar cells places them at the forefront of next-generation photovoltaics, yet scalable and reliable manufacturing routes remain a critical bottleneck. Solution processing dominates academic research, while industrial thin-film technologies are largely based on vacuum deposition. Close-space sublimation (CSS), a mature technique in chalcogenide semiconductors, offers an attractive solvent-free and high-throughput pathway, but its potential for large-area and stable perovskite devices has been scarcely explored. Here we show that CSS operated under mild vacuum enables reproducible fabrication of uniform, large-grain perovskite films across multiple substrates simultaneously, delivering nearly 19% power conversion efficiency and excellent operational stability under continuous stress. By combining simplicity, scalability, and stability, CSS establishes itself as a strong candidate for industrial adoption, bringing perovskite photovoltaics closer to commercial reality.

Introduction

In the last decade, perovskite solar cells (PSCs) have emerged as one of the most promising photovoltaic technologies, with a power conversion efficiency (PCE) surpassing 26%.[1–4] One advantage of perovskite-based semiconductors in photovoltaic applications is their tolerance to defects, which allows for simple and low-cost processing routes.[5–8] Perovskites can be fabricated using different techniques, generally classified as solution-based, dry or a hybrid of both.[9–14]

Solution-based methods are the most widely adopted, and account for the majority of the research leading to the highest PCEs in the field.[15–19] Recently, solar cells employing vacuum-processed perovskite films have also surpassed the 26% threshold.[20] Vacuum processing relies on the thermal evaporation of the solid precursors, which can be carried out simultaneously with co-evaporation, but also sequentially, in a two-step approach. In sequential deposition methods, inorganic precursors are deposited first *via* thermal evaporation and are then converted to the perovskite by applying the organic precursor(s) in a second sublimation step.[21,22] In hybrid methods, organic precursors are applied onto a vacuum deposited inorganic film *via* a solution-based technique, or *vice versa*.[11] Dry vacuum processing offers advantages for industrial-scale fabrication, including the elimination of solvents, precise control over perovskite film thickness and composition, and the capability to construct multilayer architectures.[23,24] However, even in recent reports of fast thermal deposition, it is a rather slow process.[23,25,26] In co-sublimation, compositional control is challenging, in particular for multi-cation and -anion perovskites as the sublimation rates of all precursors must be controlled simultaneously.[27–30] In sequential or two-step methods, usually, only the inorganic components are co-sublimed, allowing for an easier control of the composition as they have more stable evaporation rates.

Close-space sublimation (CSS) is an industrial method to prepare thin-film semiconductors.[31] In CSS, the substrate is

Instituto de Ciencia Molecular, Universidad de Valencia, C/Catedrático J. Beltrán 2, 46980 Paterna, Spain. E-mail: lidon.gil@uv.es; henk.bolink@uv.es

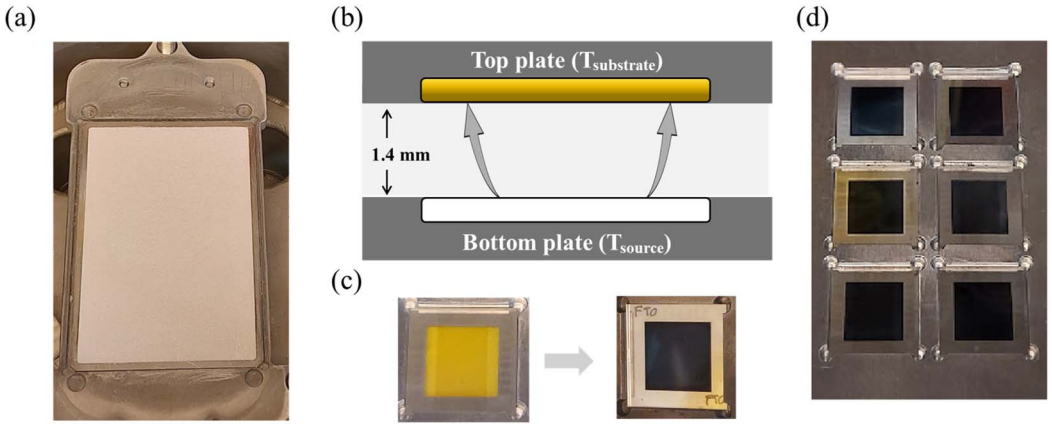

Fig. 1 (a) Bottom plate with the tempered organic source. (b) Schematic of the conversion process from the inorganic precursor film (positioned on the top plate) and the organic cation located in the cuvette placed on the bottom plate, separated by 1.4 mm. (c) Colour change of the inorganic precursor film from yellow (lead iodide) to dark (perovskite) indicating its effective conversion. (d) Uniform dark coloration of the six samples that have been converted simultaneously in the same process.

placed in close proximity to the source. As the distance that the vapour needs to overcome is small, it can operate at moderate vacuum levels.[32] When CSS is applied for the fabrication of perovskite films, the inorganic precursor layer is converted to perovskite by placing it in close proximity (typically 1–2 mm) to the organic precursor. The CSS technique has been employed for perovskite deposition, offering a promising route for scalable fabrication. In some studies, configurations classified as CSS have been implemented where the organic source is not recovered during the process, which may pose certain limitations regarding material utilization and long-term sustainability.[33–36] Nevertheless, other approaches have demonstrated the feasibility of the CSS technique in which the organic source is reusable, contributing to more resource-efficient and potentially cost-effective processing.[37–39] Recently, using a custom-made small-area CSS system with individually controlled source and substrate heaters, our group demonstrated the fabrication of an efficient fully evaporated n–i–p perovskite solar cell.[40] This was achieved using a reusable source of the organic perovskite precursor salt, formamidinium iodide (FAI), where the FAI powder was compressed into a pellet. In this study, a large area (96 cm^2) CSS tool has been used to prepare methylammonium lead iodide (MAPI) perovskites. This allows simultaneous deposition of the perovskite on six 3 by 3 cm substrates with high spatial uniformity. When integrated into thin-film solar cells, these films yielded devices with minimal performance variation per substrate. Using this method, we achieved p–i–n perovskite solar cells with a power conversion efficiency (PCE) of 18.8% and remarkable stability; they retain 90% of their initial efficiency after operating for 1000 hours at their maximum power point at 75 °C and under 1 sun illumination.

Results and discussion

We developed a large area CSS tool capable of accommodating substrates up to 96 cm^2 which was used to simultaneously deposit perovskite films on 6 substrates with dimensions of 3 × 3 cm^2; further details of the tool are shown in Fig. S1. The system consists of three plates, which hold the organic source, the substrates, and the source and substrate heaters. It is important to mention that both the top and bottom plates are equipped with separate heaters and independent temperature controllers. In our previous small-area setup, a pressed pellet of the organic perovskite precursor salt was used as the source. Consequently, for this larger tool we fabricated larger pellets, designed to cover the entire coating area (see Fig. S2a). However, the large pellets bend after only a few depositions cycles due to thermal stress. This leads to a non-uniform distance between the source and the heater, limiting reproducibility and homogeneity of the deposition process (Fig. S2b and c). Therefore, we spread the organic perovskite precursor salt powder in a large area cuvette with the same dimensions as the source heater. The procedure for preparing the organic source is shown in Fig. S3. The powder is uniformly distributed and heated at 100 °C, initially at atmospheric pressure, followed by a reduction to 1 mbar. Once tempered, the source material is homogeneous and compact (Fig. 1a), and can be used for multiple deposition cycles.

We employed fluorine tin oxide (FTO) coated glass substrates for the conversion process. Prior to the thermal sublimation of the 200 nm PbI_2 inorganic scaffold, a thin film (1.5 nm) of (2-(3,6-dimethoxy-9*H*-carbazol-9-yl)ethyl)phosphonic acid (MeO-2PACz) was deposited on the FTO substrate, acting as the hole transport layer (HTL). Both MeO-2PACz and PbI_2 were sublimed in dedicated high vacuum chambers integrated in inert gloveboxes.[41] The next step involves the conversion of PbI_2 to MAPI within the CSS tool by subliming MAI, according to the schematic process shown in Fig. 1b. The source and substrate are heated to the targeted temperature, and the conversion starts when the pressure is reduced from atmospheric pressure to 1 mbar. This conversion process ceases upon restoring the pressure to atmospheric levels. This method allows for precise control of the conversion time in the CSS system. Fig. 1c

illustrates the visual transformation of the films, transitioning from the characteristic yellowish colour of the PbI_2 layer to the dark-brown-colour of the MAPI perovskite film, a first indication that the conversion has taken place. Since all the substrates exhibit a uniform dark coloration as observed in Fig. 1d, it appears that the temperature is uniform across the bottom and top plates. This implies that large area substrates can be used, or, as in our case multiple substrates can be converted simultaneously.

In CSS, multiple parameters influence the conversion process. These include the gap between the source and the substrate, their temperatures, the thickness and composition of the inorganic layer, as well as the type of the source material. Using a gap of 1.4 mm and a working pressure of 1 mbar, we varied the source temperature (T_{source}) to evaluate the effect on the perovskite growth. In particular, T_{source} of 80, 90 and 100 °C were evaluated using 30 min conversion time. The X-ray diffraction (XRD) patterns of the resulting perovskite films are displayed in Fig. S4 of the SI. Insufficient source and substrate temperature results in an excess of MAI content and almost no appearance of the perovskite diffraction peaks. The optimal conditions for the perovskite formation were found when the source was heated to 100 °C.

To shorten the processing time, T_{source} can be increased to 120 °C, so that the perovskite formation is completed after 5 min conversion, see Fig. S5. Even though these short conversion times are one of the benefits of CSS for perovskites, it does make reproducibility in this batch process more challenging. Shorter times, imply that the start and end of the deposition of the MAI need to be well controlled as this determines the stoichiometry of the final perovskite. With slightly prolonged deposition times, the start and end times are slightly less critical. This issue would be removed if the current batch process would be converted to a continuous process. Therefore, to enable better batch-to-batch reproducibility, a slightly longer reaction time is desirable. This is the reason why in this study, T_{source} was kept maximum at 100 °C and three different conversion times were investigated, 25, 30, and 35 minutes.

Using the following settings, a gap of 1.4 mm, PbI_2 at the substrate with a thickness of 200 nm, MAI as the source material, $T_{source} = 100$ °C, and the three conversion times, different perovskite films were obtained. The films were characterized by XRD, optical absorption and scanning electron microscopy (SEM). Fig. 2a presents the XRD patterns for the three different conversion times: 25, 30, and 35 minutes. The XRD data show no peak at 12.5°, which corresponds to lead iodide, indicating the complete conversion of the inorganic precursor layer. This absence of residual lead iodide confirms that all three reaction times effectively transformed the material into the perovskite phase. The consistency in phase formation across different reaction times suggests that there is a wide window in the conversion process that allows for obtaining the perovskite films. These results highlight the efficiency of the method in achieving a fully crystallized perovskite structure. Fig. 2b presents the UV-Vis absorption spectra of the perovskite films prepared at the three different reaction times. The spectra

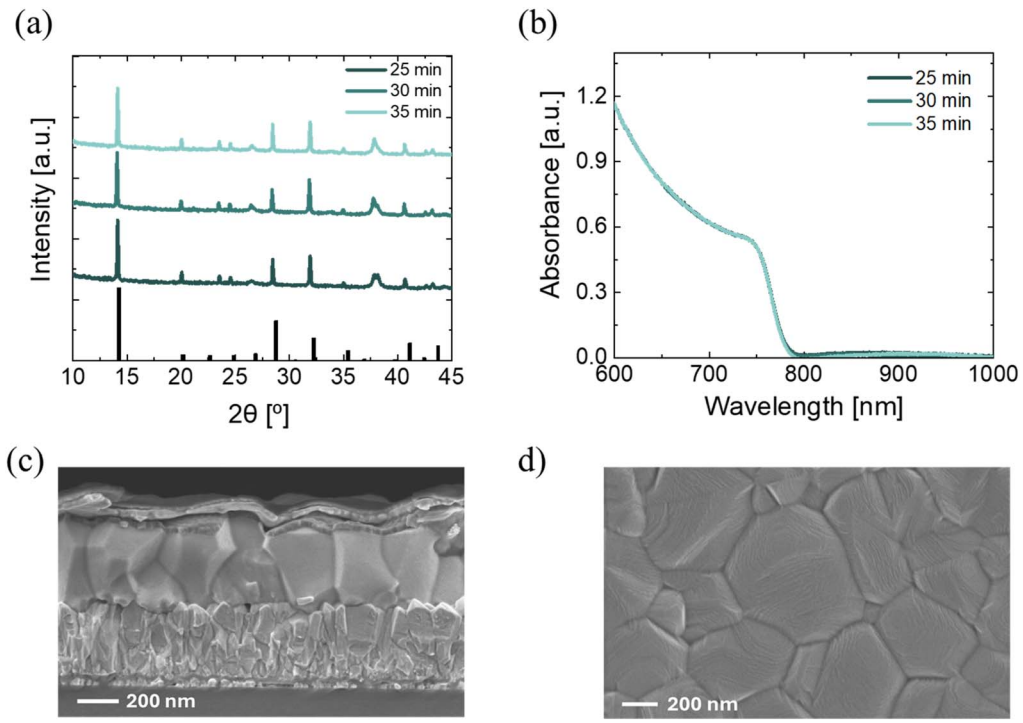

Fig. 2 (a) XRD patterns for perovskite films processed at different conversion times (25, 30, and 35 minutes), compared to a reference cubic pattern. (b) UV-Vis absorption spectra of the perovskite films obtained with the three different conversion times. (c) Cross-sectional SEM image of a solar cell containing the perovskite film processed with the 30 min conversion time and (d) the top-view SEM image of the perovskite film processed with the 30 minute conversion time.

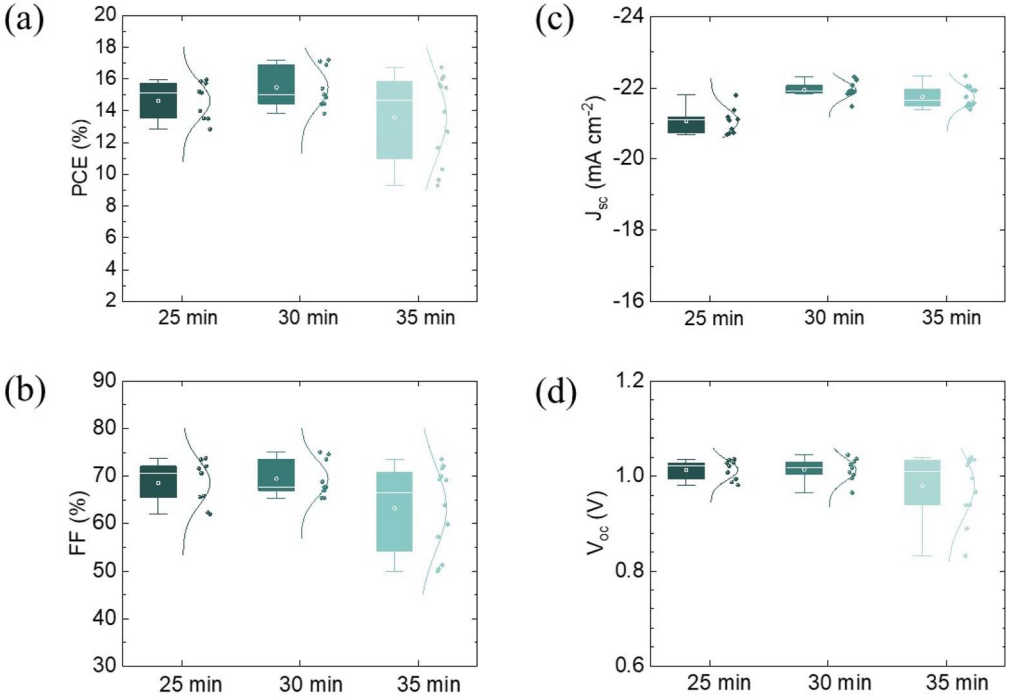

Fig. 3 Performance statistics extracted from the *JV* curves obtained under simulated solar illumination for devices that have been converted using the 25 min, 30 min and 35 min processes. (a) PCE (b) FF (c) J_{sc}, and (d) V_{oc}.

exhibit a sharp absorption edge around 780 nm, characteristic of the MAPI perovskite. The nearly identical absorption profiles suggest that all three films have similar optical properties, indicating that the variations in reaction time do not significantly affect the light absorption behaviour of the material. This suggests that the CSS process allows flexibility in the conversion time with a window of conversion of at least 10 minutes. In the cross-section SEM image, Fig. 2c, we can observe the grain size and morphology of the perovskite film of a completed device obtained with the 30 minute process. The perovskite film has a uniform thickness of 370 nm with columnar grains that grow as thick as the perovskite film. The absence of voids or defects suggests good film quality and effective materials conversion. A representative top-view SEM image of the perovskite film is displayed in Fig. 2d. The surface morphology reveals grain sizes consistent with those observed in the cross-sectional analysis, with dimensions exceeding 200 nm. These grains are significantly larger than what is usually obtained for perovskites deposited using thermal co-sublimation in a high vacuum as shown in Fig. S6.[23] To test the electrical properties of these thin films, we used the steady-state photo-carrier grating technique (SSPG),[42] achieving an in plane minority carrier diffusion length of $L_d \approx 0.33$ μm, which is on par with reported values for perovskite thin films.[43,44] Co-sublimed $MAPbI_3$ films fabricated during the same period exhibit slightly shorter diffusion lengths compared to those produced *via* the CSS method. This difference may be attributed to the larger grain sizes typically achieved with CSS, which can enhance charge transport. This effect is particularly relevant given that SSPG measurements probe in-plane diffusion lengths.

The CSS grown MAPI films were used to prepare fully-vacuum processed solar cells in a p–i–n configuration with the following structure: glass/FTO/MeO-2PACz/MAPI/C_{60}/BCP/Ag, where C_{60} is fullerene and BCP is bathocuproine, which were used as electron transport layers (ETLs) and were deposited using thermal sublimation in a high-vacuum chamber. Ag was used as the top contact and the devices were encapsulated with Al_2O_3 using atomic layer deposition (ALD). Detailed information on device fabrication, characterization, and materials is included in the Experimental section.

Solar cells containing the three different perovskites, with the three processing times were characterized using current density voltage (*JV*) scans in the dark and under simulated AM1.5G solar illumination. The *JV* curves are displayed in Fig. S8 in the SI and the key performance parameters extracted from these *JV* curves are displayed in Fig. 3. While the results are rather similar, the 30 minute process stands out with the highest PCEs. The longer processing times are beneficial for the short-circuit current density (J_{sc}), with values of 21.9 and 21.8 mA cm^{-2} for the 30 and 35 minute processes, respectively. In contrast, shorter processing times lead to slightly better open-circuit voltage (V_{oc}) and fill factor (FF), with the 25 and 30 minute samples outperforming the 35 minute process. Specifically, the V_{oc} shows a difference of 35 mV between the shortest and longest times, while the FF shows an average improvement of 5–6%. Hence, the 30 minute process is the most suitable in terms of efficiency.

The external quantum efficiency (EQE), *JV* curve under 1 sun illumination and maximum power point (mpp) tracking of the best performing pixel of the devices processed for 30 minutes

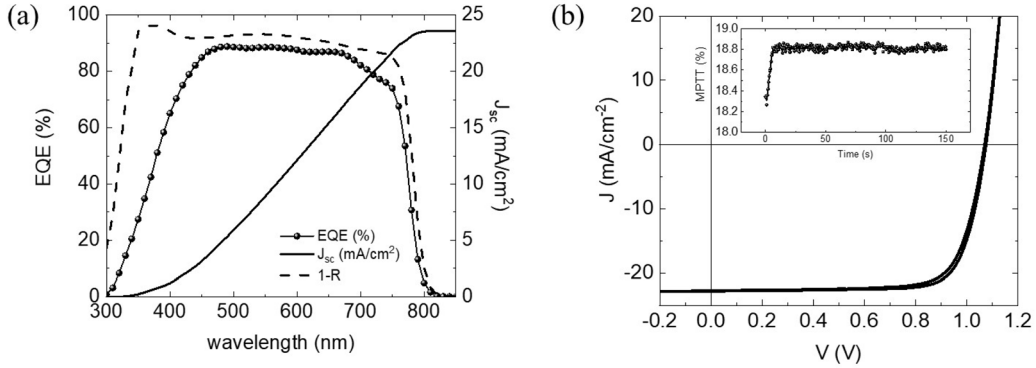

Fig. 4 (a) External quantum efficiency and 1-reflectance curves. (b) *JV* curve for the best pixel with stabilized power output measured for 100 s in the inset.

are displayed in Fig. 4. The data were obtained after having been stored for seven days under inert conditions, in ambient light and at room temperature. These conditions improve the performance slightly, something that we observed previously for co-evaporated perovskite-based devices.[45] The EQE shows a plateau between 450 and 700 nm with values approaching 90%. The integrated current density calculated from the EQE spectrum is 23.6 mA cm^{-2}, which is slightly higher than the value obtained from the *JV* curve under simulated solar illumination. This is somewhat opposite to the most general trend (J_{sc} from *JV* being higher), but not unusual and likely related to the very different light intensity used in the two measurements.[46] In the region between 700 and 770 nm, the EQE slightly diminishes, due to the limited thickness of the perovskite film (370 nm extracted from the SEM cross-section). On the same graph the 1-*R* spectrum is represented, showing a 5% loss in reflectance and an offset of approximately 10% between EQE and 1-*R*, indicating losses in charge collection within the perovskite layer.[47] Fig. 4b shows the *JV* curve from the best pixel measured after 7 days. The performance improved reaching a PCE of 18.8%, V_{oc} of 1.08 V, J_{sc} of 22.8 mA cm^{-2} and FF of 77%. The inset provides a magnified view of the stabilized power output, showing a stable power generation under steady-state conditions at 18.8%.

Using the process described above (a working pressure of 1 mbar, source/substrate temperatures of 100/120 °C, and a conversion time of 30 minutes), we then went on to evaluate the prospect of our CSS method for larger-area perovskite deposition. In particular, we want to determine the pixel to pixel variation for 6 substrates (3 by 3 cm in size) that are simultaneously converted in our CSS system. In the previous devices an evaporated layer of MeO-2PACz was used with a thickness of 1.5 nm. This is a rather thin film and variations in its thickness lead to strong effects on the device performance. For this reason, we used an alternative hole transport layer that is less sensitive to the thickness variation. This HTL is a bilayer

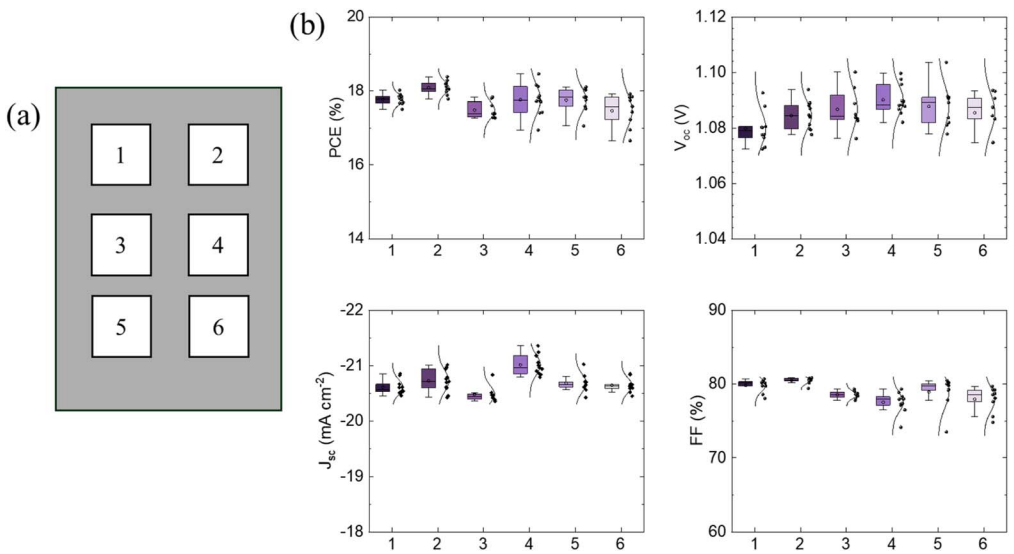

Fig. 5 (a) Bottom plate with the device layout of the six samples. (b) Performance statistics for the devices that have been converted: PCE, V_{oc}, J_{sc}, and FF.

consisting of a 20 nm layer of a partially oxidized arylamine, *N*,*N*,*N*′,*N*′-tetra([1,1′-biphenyl]-4-yl)[1,1′:4′,1″-terphenyl]-4,4″-diamine (TATM) doped with the oxidant CS90112 covered by 10 nm of an intrinsic layer of TATM. This bilayer HTL has been used by our group in many previous reports.[48] The details of the preparation of this layer are described in the Experimental section. Six substrates containing this bilayer HTL and a 200 nm layer of PbI_2 were prepared and processed simultaneously under the same conditions with the CSS tool. After the conversion to perovskites, the stacks were completed into solar cells by the evaporation of C_{60}/BCP and Ag as the ETL and top electrode, respectively (same as for the devices using the MeO-2PACz HTL).

Fig. 5a illustrates the positions of the six devices during the conversion process in the CSS system, numbered from 1–6. The corresponding device parameters are presented in Fig. 5b. All devices exhibited similar performance, with a mean PCE value of approximately 17.5% and a standard deviation of ±0.6. V_{oc} values fluctuate slightly around an average of 1.09 V, with a deviation of ±0.01 V. J_{sc} shows minimal variations, averaging 20.2 mA cm^{-2} ± 0.3 mA cm^{-2}. And the FF exhibits a slightly higher variability, averaging 78% ± 2%. The similarity of the power conversion efficiency (PCE) values to those of the top-performing pixel shown in Fig. 4 confirms the robustness of the process, underscoring its potential for high-throughput fabrication of large-area perovskite solar cells. Furthermore, negligible hysteresis was observed between the forward (negative-to-positive bias) and reverse *JV* scans, regardless of the scan rate employed (Fig. S9 and Table S1).

The stability of the solar cells incorporating the bilayer hole transport layer (HTL) and the perovskite absorber fabricated *via* the CSS method was systematically evaluated. We employed a custom-built lifetime setup consisting of an LED array and a temperature-controlled hotplate to monitor the maximum power point (mpp) evolution of the CSS-fabricated devices over time (Fig. S10). As this system operates under ambient conditions, the solar cells were encapsulated using a UV curable resin and a top cover glass (Fig. S11). Copper wires were soldered to the contact pads prior to the application of the resin to enable contacting the individual pixels. This contacting and encapsulation procedure does not notably alter the performance of the cells, as verified by *JV* scans under simulated AM1.5G sunlight (Fig. 6a). The cells were maintained at maximum power point at 75 °C and at a light intensity equivalent to 1 sun.

Fig. 6a displays *JV* characteristics of a perovskite solar cell at different stages of encapsulation and thermal/light stress testing. The red curve represents the device performance *as-deposited*, while the pink curve shows the response *after encapsulation*, indicating minimal performance loss from the encapsulation process. Subsequently, the device was subjected to a maximum power point (mpp) tracking stability test at 75 °C under continuous 1 sun illumination. The dark blue curve corresponds to the *JV* measurements taken after 0 hours (t_0) of mpp tracking operation; there was a loss in V_{oc} when the solar cell was at elevated temperature despite the cell being freshly fabricated. This is expected from the diode equations and from the temperature coefficient of the V_{oc} in perovskites, and also because the bandgap of perovskites increases with temperature.[49]

Fig. 6b shows the evolution of the normalized power output of the perovskite solar cells over more than 1000 hours under continuous mpp tracking at 75 °C and 1 sun equivalent illumination. The power output remains remarkably stable, with only a slight decrease over time. The normalized evolution of the J_{sc} and V_{oc} extracted during mpp tracking is depicted in Fig. 6c. Negligible degradation in V_{oc} and only a minor decrease over time in the J_{sc} were observed, indicating excellent operational stability under prolonged thermal and light stress. The minor fluctuations observed are within typical experimental variations, and the power output retains over 90% of its initial value, confirming the robustness of the device. This is one of the best reported stabilities for a MAPI-based solar cell, demonstrating the excellent properties of the CSS processed perovskite film.

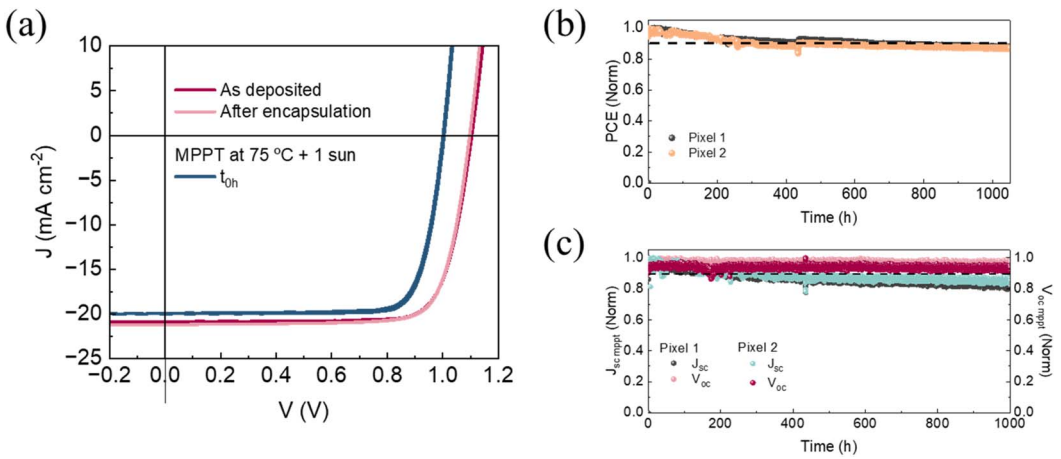

Fig. 6 (a) *JV* curves measured at different stages: as-deposited, after encapsulation, and after mpp tracking testing at 75 °C under 1 sun illumination at t_0. (b) Normalized power output of the device during mpp tracking operation of two different pixels. (c) Normalized evolution of J_{sc} and V_{oc} during mpp tracking of two different pixels.

Conclusion

This study highlights the potential of close-space sublimation (CSS) as a scalable, solvent-free method for fabricating high-quality perovskite films. By employing a large, reusable tempered source (96 cm^2), the process achieves high reproducibility, reduced material waste, and simplified operation without the need to reload organic precursors for each run. The conversion is fast, occurs at low vacuum (1 mbar), and enables the simultaneous preparation of multiple perovskite films with uniform coverage and large-grains. The resulting solar cells deliver a power conversion efficiency (PCE) of 18.8% and exhibit impressive thermal and operational stability. They retain 90% of their initial efficiency after operating for 1000 hours at their maximum power point at 75 °C and under 1 sun illumination. These results position CSS as a promising route for sustainable and scalable perovskite photovoltaics.

Methodology

Materials

Fullerene (C_{60}) was purchased from CreaPhys. TATM was obtained from Tokyo Chemical Industry (T.C.I). PbI_2, MAI, MeO-2PACz, BCP and CS90112 were purchased from Luminescence Technology Corp. All materials were used as received.

Tempered source preparation

20 g of methylammonium iodide (MAI) was ground and spread onto the evaporation source. After leveling, the source and powder were heated for 1 hour at 100 °C under atmospheric pressure inside a nitrogen filled glovebox, followed by an additional 1 hour treatment at 100 °C under a reduced pressure of 1 mbar. Upon completion of this process, the source was used for the CSS perovskite processing steps.

Device preparation

FTO-coated glass substrates were subsequently cleaned with soap (2% Mucasol™ in water), water and isopropanol in an ultrasonic bath, followed by 20 min UV-ozone treatment. The substrates were transferred to a vacuum chamber integrated in an inert nitrogen-filled glovebox and evacuated to a pressure of 10^{-6} mbar for the charge extraction layers' deposition. One chamber was used to sublime MeO-2PACz, TATM, CS90112, C_{60} and BCP. 1.5 nm of MeO-2PACz was deposited with a deposition rate of 0.2 Å s^{-1}. For the bilayer HTL, 20 nm of the p-doped HTL (TATM:CS90112) capped with 10 nm of the intrinsic TATM was deposited. The deposition rate of TATM was 0.8 Å s^{-1}, while CS90112 was deposited at 0.2 Å s^{-1}. A 200 nm PbI_2 inorganic layer was evaporated in a dedicated vacuum chamber integrated in an inert nitrogen-filled glovebox. All sources have a dedicated QCM sensor above and the PbI_2 material was loaded in an alumina crucible. Afterwards, the substrates were transferred to the close-space chamber for the perovskite conversion. The temperatures were set at 100 °C for the source and for the substrates, with a pressure of 1 mbar. Three different conversion times were investigated: 25, 30 and 35 min. After the perovskite conversion, the perovskite films were washed with 100 μL isopropanol by spincoating at 3000 rpm for 30 s, followed by 2 min annealing at 100 °C inside a glovebox. 25 nm of C_{60} was deposited with a sublimation rate of 0.5 Å s^{-1}, while 7 nm of the BCP layer was deposited at 0.2 Å s^{-1}. Ag was deposited in a third vacuum chamber also integrated in an inert nitrogen-filled glovebox from alumina-coated aluminium boats, by applying currents ranging from 2.0 to 4.5 A. All devices were coated with Al_2O_3 (30 nm) by atomic layer deposition (Arradiance's GEMStar XT Thermal ALD) prior to characterization, which was carried out in an ambient atmosphere. Transfer of the substrates from the different processing chambers was done *via* a hermetically sealed vacuum tube to prevent exposure to ambient conditions.

Device encapsulation for the MPP tracking measurements

To connect the device to the MPP tracking system, 4 copper wires (CUL100/0.35) were soldered to the device using an ultrasonic soldering system (9210 MkII AIR) with lead-free soldering wires (Cerasolzer GS-155) at 200 °C. The device was then encapsulated by applying a thick layer (~1 mm) of Eversolar® AB-341 UV curable resin from Everlight Chemicals on the device, and then covered with a glass substrate, as shown in Fig. S10. The UV resin was then cured with UV light ($\lambda = 360$ nm) for 6 minutes. For all measurements, a metal mask was used to ensure that the active area of the pixels was 0.1 cm^2.

Materials characterization

Absorption spectra were collected using a fiber optics-based Avantes Avaspec-2048 spectrometer. The XRD patterns were collected in Bragg–Brentano geometry on an Empyrean PANalytical powder diffractometer with a copper anode operated at 45 kV and 40 mA. Scanning Electron Microscopy (SEM) was performed with a high-resolution field-emission Hitachi SU8010 microscope operating at an accelerating voltage of 2 kV over platinum-metallized samples. Steady state photocarrier grating (SSPG) measurements were carried out using a He–Ne laser with 15 mW power and 632 nm wavelength. Samples for SSPG consisted of perovskite films deposited on glass, coated with two 5 mm wide Au electrodes separated by a 0.5 mm gap. Using neutral density filters, a generation rate of 3×10^{21} (cm^{-3} s^{-1}), which is close to 1 sun equivalent intensity, was obtained.

Device characterization

JV curves were recorded using a Keithley 2612A SourceMeter in the −0.2 to 1.2 V voltage range, with 0.01 V steps and integrating the signal for 20 ms after a 10 ms delay, corresponding to a scan speed of about 0.3 V s^{-1}. A device layout of 0.0825 cm^2 was used to test the solar cells measured through a shadow mask with an aperture area of 0.05 cm^2. For the hysteresis study, different scan rates (0.1, 0.5 and 1 V s^{-1}) were used, biasing the device from −0.2 to 1.2 V with 0.01 steps and *vice versa*. The devices were illuminated with a Wavelabs Sinus-70 LED solar simulator, see spectra in Fig. S12. For the absolute calibration of the solar simulator we used a silicon calibrated cell provided by Abet, with a KG5 window that mimics the bandgap of the perovskite

giving a mismatch correction factor of $M = 1.05$. EQE measurements were performed on a QE-R system from Enlitech. The system was calibrated and the solar spectrum mismatch was corrected using a calibrated silicon reference cell.

MPP tracking indoor measurements

Our indoor measurements were performed using a Kelwood Parker 3 series lamp (par3-100-750-110) as the light source, and a Stuart SD160 digital hotplate as the heat source. The hotplate has an iron device holder, where the devices can be placed and fixed. A schematic and a picture of our indoor setup are shown in Fig. S9. The light source was calibrated using both a Si reference cell with a KG5 filter (RR-239-KG5) and a fresh perovskite device. To perform the calibration, we first measured the current output of both reference devices using an AA solar simulator (Newport LSH-7320 series) under 1 sun illumination. We then measured the current output of the devices under the light source at the same height as the hotplate, and we increased its light intensity to make it match the currents measured in the reference devices under the solar simulator. To keep the temperature of the hotplate at 75 °C we used two independent methods. First, we set the temperature of the hotplate at 80 °C, to maintain the desired temperature on its surface. Then, we periodically checked the temperature of the device using a RS 206-3722 sensor (see Fig. S10c). The tip of the thermocouple was encapsulated using the procedure described before for the cell, but by dyeing the UV curable resin black, to mimic the color of a photovoltaic device. The temperature measurements were made placing the encapsulated sensor on the hotplate holder, and keeping the device for 2 hours, as depicted in Fig. S10c. The maximum power point was tracked using a 24 channel μMPP tracking system (Model: MP0210M24), acquired from the University of Ljubljana. The *J–V* curves at 75 °C were measured using a Ossila Xtralien X200 source measure unit.

Conflicts of interest

There are no conflicts to declare.

Data availability

Data from the manuscript is available at the University of Valencia's repository Roderic (**https://roderic.uv.es/**) and the European repository Zenodo (**https://zenodo.org/records/17414694**).

Supplementary information is available. See DOI: **https://doi.org/10.1039/d5el00145e**.

Acknowledgements

We acknowledge Jorge Ferrando for his help with the lifetime setup. This work was funded by the European Union; views and opinions expressed are however those of the authors only and do not necessarily reflect those of the European Union or ERCEA; neither the European Union nor the granting authority can be held responsible for them. The APERITIF project has received funding from the Horizon Europe Research and Innovation Action programme under Grant Agreement No. 101075330. This study forms part of the Advanced Materials programme and was supported by MCIN with funding from European Union NextGenerationEU (PRTR-C17.I1) and by Generalitat Valenciana (MFA/2022/022). C. R.-C. acknowledges the Ministry of Science and Innovation (MCIN), and the Spanish State Research Agency (AEI): Grant RYC2019-027187-I funded by MCIN/AEI/10.13039/474 501100011033 and by "ESF Investing in Your Future". M. S. acknowledges support from the Generalitat Valenciana (CISEJI/2022/43).

References

1 M. M. Lee, J. Teuscher, T. Miyasaka, T. N. Murakami and H. J. Snaith, *Science*, 2012, **338**, 643–647.
2 S. Liu, J. Li, W. Xiao, R. Chen, Z. Sun, Y. Zhang, X. Lei, S. Hu, M. Kober-Czerny, J. Wang, F. Ren, Q. Zhou, H. Raza, Y. Gao, Y. Ji, S. Li, H. Li, L. Qiu, W. Huang, Y. Zhao, B. Xu, Z. Liu, H. J. Snaith, N. G. Park and W. Chen, *Nature*, 2024, **632**, 536–542.
3 M. Li, B. Jiao, Y. Peng, J. Zhou, L. Tan, N. Ren, Y. Ye, Y. Liu, Y. Yang, Y. Chen, L. Ding and C. Yi, *Adv. Mater.*, 2024, **36**, 9.
4 J. Y. Kim, J.-W. Lee, H. S. Jung, H. Shin and N.-G. Park, *Chem. Rev.*, 2020, **120**, 7867–7918.
5 T. M. Brenner, D. A. Egger, L. Kronik, G. Hodes and D. Cahen, *Nat. Rev. Mater.*, 2016, **1**, 15007.
6 S. D. Stranks, G. E. Eperon, G. Grancini, C. Menelaou, M. J. P. Alcocer, T. Leijtens, L. M. Herz, A. Petrozza and H. J. Snaith, *Science*, 2013, **342**, 341–344.
7 T. Jesper Jacobsson, J.-P. Correa-Baena, M. Pazoki, M. Saliba, K. Schenk, M. Grätzel and A. Hagfeldt, *Energy Environ. Sci.*, 2016, **9**, 1706–1724.
8 T. Abzieher, D. T. Moore, M. Roß, S. Albrecht, J. Silvia, H. Tan, Q. Jeangros, C. Ballif, M. T. Hoerantner, B.-S. Kim, H. J. Bolink, P. Pistor, J. C. Goldschmidt, Y.-H. Chiang, S. D. Stranks, J. Borchert, M. D. McGehee, M. Morales-Masis, J. B. Patel, A. Bruno and U. W. Paetzold, *Energy Environ. Sci.*, 2024, **17**, 1645–1663.
9 S. Lee, N.-G. Park and H. S. Jung, *MRS Bull.*, 2024, **49**, 1265–1274.
10 O. Malinkiewicz, A. Yella, Y. H. Lee, G. M. M. Espallargas, M. Graetzel, M. K. Nazeeruddin and H. J. Bolink, *Nat. Photonics*, 2014, **8**, 128–132.
11 F. Fu, L. Kranz, S. Yoon, J. Löckinger, T. Jäger, J. Perrenoud, T. Feurer, C. Gretener, S. Buecheler and A. N. Tiwari, *Phys. Status Solidi*, 2015, **212**, 2708–2717.
12 E. Aydin, E. Ugur, B. K. Yildirim, T. G. Allen, P. Dally, A. Razzaq, F. Cao, L. Xu, B. Vishal, A. Yazmaciyan, A. A. Said, S. Zhumagali, R. Azmi, M. Babics, A. Fell, C. Xiao and S. De Wolf, *Nature*, 2023, **623**, 732–738.
13 M. Saliba, T. Matsui, K. Domanski, J.-Y. Seo, A. Ummadisingu, S. M. Zakeeruddin, J.-P. Correa-Baena, W. R. Tress, A. Abate, A. Hagfeldt and M. Grätzel, *Science*, 2016, **354**(6309), 206–209.

14 L. Tan, J. Zhou, X. Zhao, S. Wang, M. Li, C. Jiang, H. Li, Y. Zhang, Y. Ye, W. Tress, L. Ding, M. Grätzel and C. Yi, *Adv. Mater.*, 2023, **35**, 2205027.
15 Y. Yang, H. Chen, C. Liu, J. Xu, C. Huang, C. D. Malliakas, H. Wan, A. S. R. Bati, Z. Wang, R. P. Reynolds, I. W. Gilley, S. Kitade, T. E. Wiggins, S. Zeiske, S. Suragtkhuu, M. Batmunkh, L. X. Chen, B. Chen, M. G. Kanatzidis and E. H. Sargent, *Science*, 2024, **386**, 898–902.
16 X. Zheng, Y. Hou, C. Bao, J. Yin, F. Yuan, Z. Huang, K. Song, J. Liu, J. Troughton, N. Gasparini, C. Zhou, Y. Lin, D.-J. Xue, B. Chen, A. K. Johnston, N. Wei, M. N. Hedhili, M. Wei, A. Y. Alsalloum, P. Maity, B. Turedi, C. Yang, D. Baran, T. D. Anthopoulos, Y. Han, Z.-H. Lu, O. F. Mohammed, F. Gao, E. H. Sargent and O. M. Bakr, *Nat. Energy*, 2020, **5**, 131–140.
17 X. Li, D. Bi, C. Yi, J.-D. Decoppet, J. Luo, S. M. Zakeeruddin, A. Hagfeldt, M. Gratzel, J. D. Décoppet, J. Luo, S. M. Zakeeruddin, A. Hagfeldt and M. Grätzel, *Science*, 2016, **353**, 58–62.
18 F. Yang, D. Jang, L. Dong, S. Qiu, A. Distler, N. Li, C. Brabec and H.-J. Egelhaaf, *Adv. Energy Mater.*, 2021, **11**, 2101973.
19 W. Nie, H. Tsai, R. Asadpour, J.-C. Blancon, A. J. Neukirch, G. Gupta, J. J. Crochet, M. Chhowalla, S. Tretiak, M. A. Alam, H.-L. Wang and A. D. Mohite, *Science*, 2015, **347**, 522–525.
20 J. Zhou, L. Tan, Y. Liu, H. Li, X. Liu, M. Li, S. Wang, Y. Zhang, C. Jiang, R. Hua, W. Tress, S. Meloni and C. Yi, *Joule*, 2024, **8**, 1691–1706.
21 H. Li, L. Tan, C. Jiang, M. Li, J. Zhou, Y. Ye, Y. Liu and C. Yi, *Adv. Funct. Mater.*, 2023, **33**, 1–10.
22 H. Li, J. Zhou, L. Tan, M. Li, C. Jiang, S. Wang, X. Zhao, Y. Liu, Y. Zhang, Y. Ye, W. Tress and C. Yi, *Sci. Adv.*, 2022, **8**, 1–9.
23 J. Ávila, C. Momblona, P. P. Boix, M. Sessolo and H. J. Bolink, *Joule*, 2017, **1**, 431–442.
24 Q. Guesnay, F. Sahli, C. Ballif and Q. Jeangros, *APL Mater.*, 2021, **9**, 100703.
25 M. Piot, J. E. S. Alonso, K. P. S. Zanoni, N. Rodkey, F. Ventosinos, C. Roldán-Carmona, M. Sessolo and H. Bolink, *ACS Energy Lett.*, 2023, **8**, 4711–4713.
26 H. A. Dewi, E. Erdenebileg, D. De Luca, S. G. Mhaisalkar and A. Bruno, *ACS Energy Lett.*, 2024, **9**, 4319–4322.
27 I. Susic, L. Gil-Escrig, F. Palazon, M. Sessolo and H. J. Bolink, *ACS Energy Lett.*, 2022, **7**, 1355–1363.
28 L. Gil-Escrig, C. Dreessen, F. Palazon, Z. Hawash, E. Moons, S. Albrecht, M. Sessolo and H. J. Bolink, *ACS Energy Lett.*, 2021, **6**, 827–836.
29 S. Yan, J. B. Patel, J. E. Lee, K. A. Elmestekawy, S. R. Ratnasingham, Q. Yuan, L. M. Herz, N. K. Noel and M. B. Johnston, *ACS Energy Lett.*, 2023, **8**, 4008–4015.
30 V. Škorjanc, A. Miaskiewicz, M. Roß, S. Maniyarasu, S. Severin, M. R. Leyden, P. Holzhey, F. Ruske, L. Korte and S. Albrecht, *ACS Energy Lett.*, 2024, **9**, 5639–5646.
31 A. J. Ritenour, J. W. Boucher, R. DeLancey, A. L. Greenaway, S. Aloni and S. W. Boettcher, *Energy Environ. Sci.*, 2015, **8**, 278–285.
32 G. Perrier, R. Philippe and J. P. Dodelet, *J. Mater. Res.*, 1988, **3**, 1031–1042.
33 Q. Guo, C. Li, W. Qiao, S. Ma, F. Wang, B. Zhang, L. Hu, S. Dai and Z. Tan, *Energy Environ. Sci.*, 2016, **9**, 1486–1494.
34 G. Zhang, W. Luo, H. Dai, N. Li, Y. Li, Y. Peng, F. Huang, Z. Ku and Y. B. Cheng, *ACS Appl. Energy Mater.*, 2022, 3–6.
35 F. Tie, C. Duan, S. Hu, Y. Dou, Q. Tan, J. Fan, J. Lu, M. Xu and Z. Ku, *ACS Appl. Energy Mater.*, 2023, **6**, 6681–6688.
36 Q. Guesnay, F. Sahli, K. Artuk, D. Turkay, A. G. Kuba, N. Mrkyvkova, K. Vegso, P. Siffalovic, F. Schreiber, H. Lai, F. Fu, M. Ledinský, N. Fürst, A. Schafflützel, C. Bucher, Q. Jeangros, C. Ballif and C. M. Wolff, *Adv. Energy Mater.*, 2024, **14**, 1–11.
37 G. Li, J. Y. L. Ho, M. Wong and H. S. Kwok, *Phys. Status Solidi RRL*, 2016, **10**, 153–157.
38 L. Gu, S. Wang, X. Fang, D. Liu, Y. Xu, N. Yuan and J. Ding, *ACS Appl. Mater. Interfaces*, 2020, **12**, 33870–33878.
39 F. Zhao, J. Zhong, L. Zhang, P. Yong, J. Lu, M. Xu, Y. Cheng and Z. Ku, *Sol. RRL*, 2023, **7**, 2300062.
40 N. Rodkey, I. Gomar-Fernández, F. Ventosinos, C. Roldan-Carmona, L. J. A. Koster and H. J. Bolink, *ACS Energy Lett.*, 2024, **9**, 927–933.
41 A. Farag, T. Feeney, I. M. Hossain, F. Schackmar, P. Fassl, K. Küster, R. Bäuerle, M. A. Ruiz-Preciado, M. Hentschel, D. B. Ritzer, A. Diercks, Y. Li, B. A. Nejand, F. Laufer, R. Singh, U. Starke and U. W. Paetzold, *Adv. Energy Mater.*, 2023, **13**, 2203982.
42 D. Ritter, E. Zeldov and K. Weiser, *J. Non-Cryst. Solids*, 1987, **97–98**, 619–622.
43 C. Cho, S. Feldmann, K. M. Yeom, Y.-W. Jang, S. Kahmann, J.-Y. Huang, T. C. Yang, M. N. T. Khayyat, Y.-R. Wu, M. Choi, J. H. Noh, S. D. Stranks and N. C. Greenham, *Nat. Mater.*, 2022, **21**, 1388–1395.
44 I. Levine, S. Gupta, A. Bera, D. Ceratti, G. Hodes, D. Cahen, D. Guo, T. J. Savenije, J. Ávila, H. J. Bolink, O. Millo, D. Azulay and I. Balberg, *J. Appl. Phys.*, 2018, **124**(10), 103103.
45 D. Kiermasch, M. Fischer, L. Gil-Escrig, A. Baumann, H. J. Bolink, V. Dyakonov and K. Tvingstedt, *Sol. RRL*, 2021, **5**, 2100400.
46 M. Saliba, E. Unger, L. Etgar, J. Luo and T. J. Jacobsson, *Nat. Commun.*, 2023, **14**, 5445.
47 N. Rodkey, K. P. S. Zanoni, M. Piot, C. Dreessen, R. Grote, P. Carroy, J. E. Sebastian Alonso, A. Paliwal, D. Muñoz and H. J. Bolink, *Adv. Energy Mater.*, 2024, **14**, 2400058.
48 C. Momblona, L. Gil-Escrig, E. Bandiello, E. M. Hutter, M. Sessolo, K. Lederer, J. Blochwitz-Nimoth and H. J. Bolink, *Energy Environ. Sci.*, 2016, **9**, 3456–3463.
49 T. Moot, J. B. Patel, G. McAndrews, E. J. Wolf, D. Morales, I. E. Gould, B. A. Rosales, C. C. Boyd, L. M. Wheeler, P. A. Parilla, S. W. Johnston, L. T. Schelhas, M. D. McGehee and J. M. Luther, *ACS Energy Lett.*, 2021, **6**, 2038–2047.